Nanoscale

ROYAL SOCIETY OF CHEMISTRY

COMMUNICATION

View Article Online
View Journal | View Issue

Cite this: *Nanoscale*, 2020, **12**, 14441

Received 8th June 2020,
Accepted 18th June 2020

DOI: 10.1039/d0nr04346j

rsc.li/nanoscale

Nitrogen-doped hollow carbon nanoflowers from a preformed covalent triazine framework for metal-free bifunctional electrocatalysis†

Yong Zheng,[a] Shan Chen,[a] Hui Song,[a] Hele Guo,[a] Kai A. I. Zhang, *[b] Chao Zhang *[a] and Tianxi Liu [a,c,d]

Fabrication of nitrogen-doped hollow carbon nanostructures is of great importance for achieving efficient electron and ion transport as a metal-free electrocatalyst. Herein, we report a step-wise polymerization and carbonization route to prepare N-doped hollow carbon nanoflowers (N-HCNFs) with a high nitrogen content up to 5.3 at%. A preformed covalent triazine framework (CTF) network assembled on a melamine-cyanuric acid (MCA) supermolecular crystal was achieved *via* a step-wise polymerization. The subsequent carbonization was conducted to obtain hollow and porous carbon materials with a unique flower-shape. Excellent electrochemical oxygen reduction reaction (ORR) performance with a positive half-wave potential of 0.84 V (*vs.* RHE) was achieved with excellent stability and methanol resistance in alkaline media. Furthermore, for the hydrogen evolution reaction (HER), a low overpotential of 243 mV at a current density of 10 mA cm^{-2} and a small Tafel slope of 111 mV dec^{-1} in acidic media were shown.

Highly efficient, green and renewable energy conversion devices, such as metal–air batteries, fuel cells, and water splitting systems, have attracted tremendous attention lately.[1] The ORR is the heart part of fuel cells and metal–air batteries, and the HER plays a vital role in fuel cells and water splitting systems.[2–6] Due to the sluggish kinetics of the two reactions, especially the ORR, developing efficient electrocatalysts is of great importance for enhancing the efficiency. To date, Pt-based noble metal materials have been certified to be the most active catalysts towards the ORR and HER.[7] However, the crossover deactivation, stiff price and low stability of these expensive catalysts preclude their large-scale commercialization.[8] To overcome these limitations, the exploitation of low-cost, highly efficient and ultra-stable electrocatalyst materials for the electrocatalytic ORR/HER is necessary.

During the last decades, intensive research efforts have been devoted to exploiting efficient alternatives to Pt-based electrocatalysts.[9–14] NC materials are at the forefront of various competitors owing to their outstanding features of low costs, being environmentally innocuous, hierarchical porous nanostructures, nitrogen-rich active centers and high specific surface areas.[15–17] The superior catalytic activity of NC materials toward the ORR and HER originates from the substitution of C atoms by N atoms in the sp^2 lattice of the carbon matrix.[2] *Via* N doping, the electronic configuration of the carbon matrix can be further modified to form pyridinic-N and graphitic-N species, which are designated as dominant catalytic sites.[18,19] In addition to the intrinsic active sites, the catalytic properties of NC materials are strongly governed by the microstructure of the carbon matrix. Hollow nanostructures offer the advantages of easily accessible inner voids, large surface areas, short diffusion paths and low density, which are favorable for catalytic applications.[20–23] During the electrocatalytic process, the open pore structure and vast void space can greatly relieve the volume variation, facilitating charge and ion transfer within the catalyst.[24] Therefore, the NC materials embellished with hollow nanostructures could be up-and-coming electrocatalysts for both the ORR and HER. Among various preparation methods, the template method is a common way to achieve the morphological control of the hollow carbon materials.[25] Compared with conventional hard/soft templates, such as SiO_2 and PS spheres, MCA as a novel organic template displays great potential because of rich surface chemistry and being easy to remove. For instance, Jun *et al.* have prepared a three-dimensional interconnected hard

[a]*State Key Laboratory for Modification of Chemical Fibers and Polymer Materials, College of Materials Science and Engineering, Innovation Center for Textile Science and Technology, Donghua University, Shanghai 201620, P. R. China. E-mail: czhang@dhu.edu.cn*
[b]*Department of Materials Science, Fudan University, Shanghai 200433, P. R. China. E-mail: kai_zhang@fudan.edu.cn*
[c]*Key Laboratory of Synthetic and Biological Colloids, Ministry of Education, School of Chemical and Material Engineering, Jiangnan University, Wuxi 214122, P. R. China*
[d]*Key Laboratory of Materials Processing and Mold (Zhengzhou University), Ministry of Education, Zhengzhou 450002, P. R. China*

† Electronic supplementary information (ESI) available: Experimental details and additional characterization data. See DOI: 10.1039/d0nr04346j

carbon material with a finely tuned microstructure by using organic MCA crystal templates.[26,27] The material obtained using the MCA template has shown high performance in lithium/sodium batteries, indicating that specific morphologies have a crucial influence on the electrochemical performance. Apart from that, these methods are not completely controllable, probably because the precursors are only randomly stacked on the surface of the template, which will lead to structural instability. It is therefore essential but still a great challenge to fabricate hollow NC with a controllable method.

More recently, CTFs are viewed as a versatile precursor to synthesize new formulas of versatile nanocarbon materials for the ORR and HER[28–35] considering the following advantages: (1) heteroatom doped carbon can act as a catalytic center, (2) ultrahigh specific surface areas can host more active sites, and (3) abundant pore distributions can provide more mass/electron transport channels.[36–40] But the electrocatalytic performance of CTF-derived cathode catalysts is still unsatisfactory due to the structural devastation and the lack of corresponding morphology control during carbonization.[37,41] Thus, it is highly expected to enhance both ORR and HER electrocatalytic performance by coupling CTF-based materials with hollow nanostructures, but it is still a huge challenge.

In this work, we report a simple and useful route to fabricate N-doped hollow carbon nanoflowers (N-HCNFs) by a stepwise polymerization and subsequent pyrolysis procedure. The key of this strategy is to control the formation of the CTF precursor only on the surface of MCA instead of its random formation in the liquid reaction medium. During carbonization, a highly interwoven network hollow structure with a hierarchical pore architecture consisting of micro- and mesopores is generated after the volatilization of the MCA crystals. After that, the framework of the MCA is well preserved and its surface N is also doped well in the CTF-derived carbon skeletons. The optimal N-HCNF catalyst exhibits an outstanding ORR and HER electrocatalytic performance in terms of attractive potential, low Tafel slope and good stability. Moreover, when the N-HCNF catalyst is used as the air electrode to assemble zinc–air batteries, its performance exceeds that of the commercial Pt/C catalyst.

The synthetic route to the N-HCNFs includes three steps, as shown in Scheme 1. First, cyanuric chloride as the directed-monomer was covalently linked onto flower-like MCA mesocrystals *via* a simple nucleophilic substitution reaction. This step provided anchors for the controlled formation of the triazine-based frameworks on the MCA surface through covalent bonding. Second, by adding piperazine, the unique covalently assembled CTF-piperazine@MCA (CTF-PP@MCA) complexes were formed. Three complexes were prepared using different CTF/MCA mass ratios of 1/4, 1/2, and 1/1, which were then referred to as CTF-PP@MCA-1, CTF-PP@MCA-2, and CTF-PP@MCA-3, respectively. Third, the CTF-PP@MCA precursors were carbonized under an inert atmosphere to obtain the N-HCNFs. The resultant materials were denoted as N-HCNFs-*x*-*T*, where *x* means the use of CTF-PP@MCA-*X* as the precursor and *T* indicates the carbonization temperature. Thanks to the excellent thermal stability of the CTF-PP, with the thermal volatilization of the MCA crystal, the ideal complex's skeletons were well maintained and hollow flower-shaped hierarchically porous carbon with a rich N-content was obtained.

Scanning electron microscopy (SEM) was conducted to examine the morphology of the resultant materials. Fig. 1a reveals that MCA has a typical flower-shaped morphology which is composed of a pile of nanosheets. After the step-wise polymerization, a certain thickness of CTF-PP was grown on the petals of MCA and there were no scattered CTF-PP aggregates (Fig. 1b). This shows that the covalent linking in the first step is very important. It is noteworthy that flower-like MCA decomposed into organic vapor in the near-spherical composites after carbonization and CTF-PP was preserved partially, leaving only a hollow spherical-like shaped carbon skeleton (Fig. 1c). The TEM image of N-HCNF-2-1000 is displayed in Fig. 1d, which further disclosed the typical hollow morphology. A high-resolution transmission electron microscopy

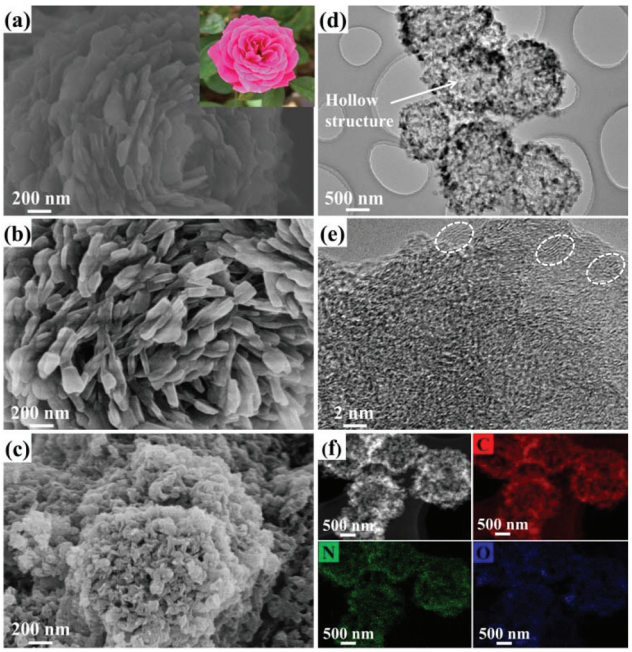

Fig. 1 SEM images of (a) MCA, (b) CTF-PP@MCA-2, and (c) N-HCNF-2-1000, (d) TEM and (e) HRTEM images of N-HCNF-2-1000, (f) TEM image of N-HCNF-2-1000 and elemental mappings, indicating uniform distributions of C, N and O in N-HCNF-2-1000.

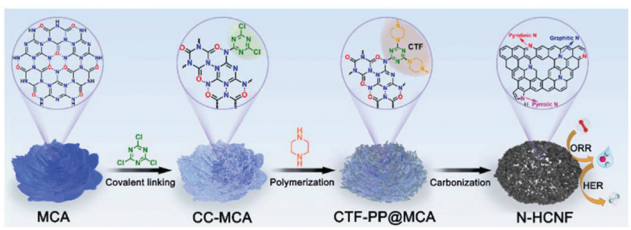

Scheme 1 Schematic illustration for the synthesis of the N-HCNFs.

(HRTEM) image (Fig. 1e) revealed relatively disordered carbon layers with multiple edge-like graphitic structures.[38] To investigate the detailed spatial distribution of nitrogen, TEM coupled with energy dispersive X-ray spectroscopy (EDS) was conducted. It can be found that C, N and O are distributed uniformly throughout the entire architecture, confirming that the surface chemical properties of the MCA were imprinted homogeneously throughout the obtained samples (Fig. 1f).

The influences of the MCA/CTF-PP mass ratio on the morphologies of CTF-PP@MCA are shown in Fig. S1.† CTF-PP@MCA-*X* complexes show several disordered layers located on the MCA surface. Also, its micromorphology was affected by the content of the CTF-PP. The optimized content of CTF-PP@MCA-2 exhibits optimal and dense CTF-PP layers which are covered on the MCA surface on the nanoscale. CTF-PP@MCA-1 exhibited thinner disordered CTF-PP layers grown on the MCA surface due to the relatively lower concentration of monomers on the MCA (Fig. S1a and b†). By contrast, we can see that CTF-PP layers are heavily stacked on the surface of MCA from the morphology of CTF-PP@MCA-3 (Fig. S1c and d†). So comparison of the SEM results shows that an optimum content of the monomer is needed in the polymerization to get appropriate CTF-PP@MCA complexes.[42] As a result, the CTF-PP@MCA complexes with a uniform size have been successfully prepared. The autonomous formation of disorderedly arranged interconnected layers along with a combination of micro-mesopores helps in the enhancement of the catalytic activity of the material. The SEM images of the N-HCNF catalysts carbonized at different temperatures are shown in Fig. S2.† At 900 °C, the hollow structure is regular, but the low graphitization is not conducive to the electron transport in the electrocatalytic process.[43,44] However, a high temperature of 1100 °C led to the collapse of the hollow structure. Therefore, the optimal carbonization temperature is 1000 °C. Besides, a combinatorial effect of hollow texture, pores, and nitrogen doping in N-HCNF-2-1000 is found to increase the number of active sites and thereby provides easy migration of channels between actives sites and the dissolved oxygen/hydrogen molecules. The hollow carbon nanoflower is expected to create more accessible catalytically active sites on the materials that can act as an ideal candidate for both the ORR and HER.[45]

To prove the first step of covalent linking, FTIR spectroscopy was used to characterize the CC-MCA obtained from the reaction of MCA with excess CC monomer. As shown in Fig. 2a, the significantly weakened N–H stretching band (3391 cm^{-1} and 3229 cm^{-1}) and obviously enhanced characteristic C–N stretching band (1221 cm^{-1}) reveal a significant decrease in $–NH_2$ groups and the successful formation of C–N covalent bonds. Fig. S3† confirmed that MCA began to decompose from 300 °C and vanished completely at approximately 450 °C. Our previous work showed that the morphology of CTF-PP can be well maintained after carbonization.[40] These two factors ensure the formation of hollow structures after carbonization. Simultaneously, the enriched N of MCA was doped in the CTF derived carbon skeleton, promoting the formation of abundant *N*-relative electrocatalytic active sites.[27]

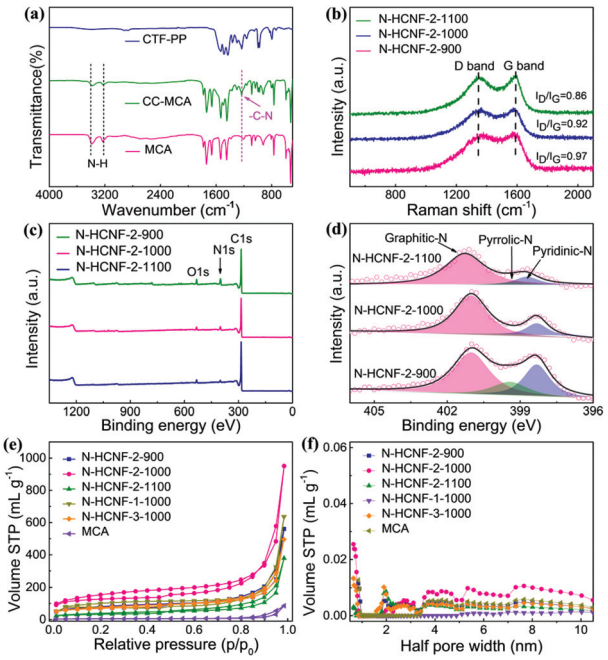

Fig. 2 (a) FT-IR spectra of CTF-PP, CTF-PP@MCA-2 and MCA, (b) Raman spectra of N-HCNF-2-900, N-HCNF-2-1000 and N-HCNF-2-1100, and (c) XPS spectra of N-HCNF samples prepared at different pyrolysis temperatures. (d) High-resolution N 1s XPS spectra of N-HCNF samples. (e) Nitrogen adsorption/desorption isotherm of corresponding samples and (f) corresponding pore size distribution.

X-ray photoelectron spectroscopy (XPS) was performed to examine the variation of the nitrogen bonding state and content in the samples depending on the different carbonization temperatures. As shown in the wide spectra of the samples, the three peaks located at 285 eV, 400 eV, and 510 eV correspond to carbon, nitrogen, and oxygen, respectively (Fig. 2c). Fig. 2d presents the high-resolution N 1s spectra of the samples prepared at different temperatures. Each spectrum can be deconvoluted into three characteristic peaks, *i.e.*, pyridinic N (398.3 eV), pyrrolic N (399.4 eV), and graphitic N (401 eV).[46] The nitrogen content in N-HCNF-2-900, N-HCNF-2-1000, and N-HCNF-2-1100 was 11.2, 5.3 and 4.0 at%, respectively. These exceptionally high values highlight the outstanding heteroatom doping efficiency of this approach. The nitrogen bonding states changed with the synthesis temperature according to the thermal stability of each state. The portion of graphitic N increased with increasing carbonization temperature while the portion of pyridinic N decreased because graphitic N is the most thermally stable bonding state. In the cases of N-HCNF-2-900 and N-HCNF-2-1000, pyridinic N and graphitic N showed the highest portion of the overall nitrogen content (Fig. S4b†). On the other hand, graphitic N possessed a dominant portion in N-HCNF-2-1100, but N-HCNF-2-1100 still had a relatively high value compared to the other N-doping methods. The large content of pyridinic and graphitic N would provide more efficient active sites to improve electrocatalysis.[47] The

surface chemical properties of the prepared samples were further studied by Fourier transform-infrared (FTIR) spectroscopy (Fig. S6†). After carbonization, the N-HCNF-2-1000 samples showed totally different spectra when compared with the MCA and CTF-PP@MCA (Fig. 2a). As indicated by the dashed lines, four characteristic peaks related to the nitrogen bonding state can be observed. The broad N–H peak at 3229 cm^{-1} weakened, as the carbonization temperature increased.[27] Similarly, the C–N peak (1150–1259 cm^{-1}) shifted to a lower wave number, indicating that the portion of graphitic N increased, which is consistent with the XPS results. The high-resolution C 1s spectra can be fitted into three different peaks (Fig. S5†). The main peak at 284.7 eV is related to typical sp^2 graphitic carbon. The two different peaks centered at 285.9 eV and 287.6 eV are attributed to different nitrogen bonding states in carbon, *i.e.*, N–sp^2C and N–sp^3C, respectively.[46]

The carbonization temperature plays a crucial role in the electrocatalytic performance by influencing the graphitization degrees.[40] For the final carbon, the intensity ratio of the D (1320 cm^{-1}) to G bands (1580 cm^{-1}),[48] indicating the degree of defects or disorders, I_D/I_G, decreased from 0.97 to 0.86 with increasing synthesis temperature (Fig. 2b). According to the previous report, defects are crucial for both the ORR and HER catalysts.[49] This observation provides robust support to confirm the successful synthesis of the catalyst which may exhibit good electrocatalytic performance. All N-HCNF samples exhibited a broad pattern at $2\theta = 25.9°$, corresponding to the (002) peak related to the degree of graphitization (Fig. S4a†). The broad (002) peak indicates the short range order along the *c*-axis of the graphitic sheets, which is usually observed in porous carbon.[29] Additionally, an additional peak at 43° equivalent to the (100) peak was observed, which is consistent with the TEM results (Fig. 2e). Owing to the much less developed in-plane graphitic ordering in porous carbon, the apparent (100) peak of the samples indicates an exceptional graphitic ordering along the axis, which might guarantee stable conducting pathways in the resulting materials.[46] This is consistent with not only FTIR but also Raman spectroscopy that reveals the degree of disorder in the carbon nanostructures (Fig. 2b).

The pore characteristics of the samples were quantified by measuring the N_2 isotherm (Fig. 2e). The Brunauer–Emmett–Teller (BET) specific surface area (SSA) and total pore volume of the samples are listed in Fig. S4c.† It was observed that the BET SSA increased remarkably from the MCA (13 $m^2\ g^{-1}$) to the N-HCNF-*x*-*T* samples (197–368 $m^2\ g^{-1}$). The isotherms of all final carbons showed a similar trend with an initial high nitrogen uptake at low relative pressures, followed by a moderate slope at intermediate relative pressures and a steep increase at high relative pressures, indicating the presence of multi-scale pores. The pore size distributions calculated using the density functional theory (DFT) method showed that enormous amounts of larger *meso*- and micropores were generated (Fig. 2f). This is consistent with the SEM and TEM images and further supports the unique morphology of the resulting materials (Fig. 1c–e). It is noted that the carbonization of CTF-PP only resulted in a large number of disorderedly stacked and nonporous carbon sheets.[40] Therefore, these results point to the fact that the carbonization of CTF-PP in the presence of the MCA mesocrystals is a facile and effective method for introducing a unique nanostructure and multiscale porosity into the final carbon material without the need for specific pore manufacturing processes.

The ORR electrocatalytic performance of the N-doped carbon materials was evaluated by the rotating ring-disk electrode technique in 0.1 M KOH solution. The commercial Pt/C is also studied for comparison. As shown in Fig. 3a, N-HCNF-2-1000 exhibits a well-defined and quasi-rectangular-shaped CV with a characteristic oxygen reduction peak at approximately 0.81 V *vs.* RHE. However, the clear peak is not visible in a N_2-saturated electrolyte, indicating a high ORR reactivity for the catalyst. Besides, the reduction potential of N-HCNF-2-1000 is more positive and obvious than those of other catalysts, indicating that it has the best catalytic performance for oxygen reduction. As shown in Table 1, the N-HCNF-2-1000 exhibits the highest half-wave potential ($E_{1/2}$) of 0.84 V, which is close to that of the state-of-the-art Pt/C catalyst. The N-HCNF-2-900 and N-HCNF-2-1100 show decreased performance compared to N-HCNF-2-1000, which can be

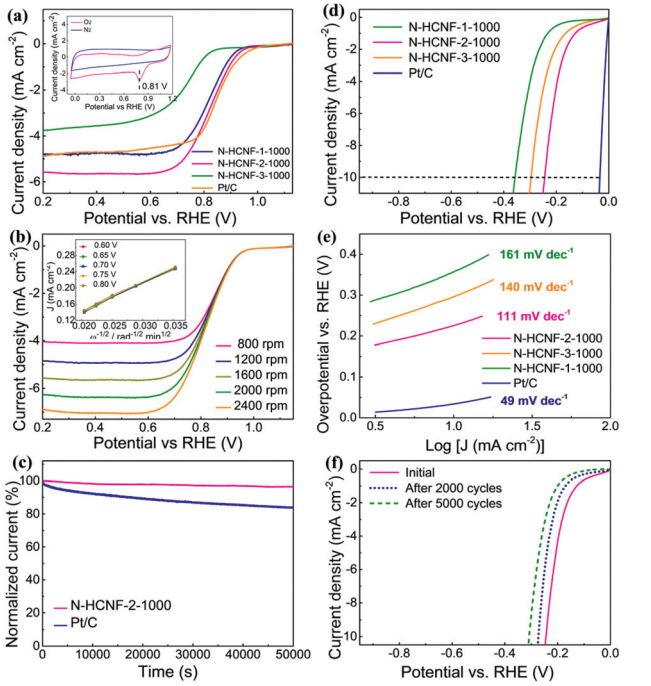

Fig. 3 (a–c) ORR performance: (a) LSV curves of N-HCNF-2-900, N-HCNF-2-1000, N-HCNF-2-1100 and Pt/C; the inset is the CV curves of the N-HCNF-2-1000 in N_2- and O_2-saturated 0.1 M KOH, respectively, (b) LSV curves of N-HCNF-2-1000 at various rotating speeds. The inset of (b) shows the K–L plots of N-HCNF-2-1000 at various potentials, (c) chronoamperometric responses of N-HCNF-2-1000 and Pt/C in O_2-saturated 0.1 M KOH. (d–f) HER performance: (d) LSV curves of N-HCNF-2-900, N-HCNF-2-1000, N-HCNF-2-1100 and Pt/C in 0.5 M H_2SO_4. (e) The Tafel curves of corresponding samples. (f) The LSV curves of N-HCNF-2-1000 before and after 5000 cycles of CV tests.

Table 1 The onset potential (E_0) and half-wave potential ($E_{1/2}$) for each catalyst

Catalyst	E_0 [V] (*vs.* RHE)	$E_{1/2}$ [V] (*vs.* RHE)	Limiting current density (mA cm^{-2})
N-HCNF-1-1000	0.97	0.82	3.77
N-HCNF-2-1000	**1.01**	**0.84**	**5.56**
N-HCNF-3-1000	0.87	0.74	3.77
N-HCNF-2-800	0.89	0.61	2.86
N-HCNF-2-900	0.96	0.79	5.54
N-HCNF-2-1100	0.95	0.79	5.62

explained by its relatively poor electrical conductivity (see Table S1†) and lower porosity, respectively. Importantly, the limiting current density of N-HCNF-2-1000 is higher than that of commercial Pt/C. The comparison with a number of previously reported metal-free carbon-based catalysts is shown in Table S2,† indicating that the electrocatalytic performance of N-HCNF-2-1000 for the ORR was comparable to that of the state-of-the-art carbon materials.

To further investigate the ORR kinetics, rotating disc electrode (RDE) measurements at different rotating speeds were carried out and the corresponding Koutecky–Levich (K–L) plots were acquired (Fig. 3b). The inset in Fig. 3b shows linear and near parallel K–L plots at different applied potentials, implying first-order reaction kinetics for the concentration of dissolved oxygen and a similar electron transfer number (n) for N-HCNF-2-1000. The N is calculated to be 3.94 at 0.8 V *vs.* RHE, suggesting that N-HCNF-2-1000 prefers a 4 e^- oxygen reduction process, that is, the direct formation of the hydroxide ion (Fig. S7c†). The Tafel curves were also plotted based on the polarization curves to assess the kinetic process of catalysts (Fig. S8a†). In the potential region of ORR catalysis, N-HCNF-2-1000 displays a Tafel slope of 81 mV dec^{-1}. The value is much smaller than that of the other as-prepared samples, and is very close to those of the Pt/C catalysts, indicating that the electron transfer in the N-HCNF-2-1000 upon catalyzing the ORR proceeds *via* a similar route to the Pt/C with the first two-electron transfer as the rate-determining step. Moreover, the corresponding calculated kinetic current densities (J_k) at 0.8 V (*vs.* RHE) are in the following order: Pt/C (10.71 mA cm^{-2}) > N-HCNF-2-1000 (7.65 mA cm^{-2}) > N-HCNF-2-1100 (4.58 mA cm^{-2}) > N-HCNF-2-900 (3.94 mA cm^{-2}) (Fig. S8c†). Rotating ring disk electrode measurements were conducted to further obtain the electron transfer number and the H_2O_2 product yields. As a result, N-HCNF-2-1000 preferably catalyzed the ORR through a four electron pathway with an electron transfer number of 3.91, which is close to that of Pt/C (3.98). Besides, charge transport is also a crucial consideration in the kinetics of the electrochemical catalytic reaction. Electrochemical impedance spectroscopy (EIS) was performed to elucidate the superior ORR activity of the obtained catalyst (Fig. S8b†). The smaller semicircle in the medium frequency region reveals the lower charge transfer resistance of the catalyst.[49] According to the Nyquist plots, the charge transfer resistance of N-HCNF-2-1000 is significantly lower than that of the other samples and Pt/C catalyst, indicating a faster charge transfer process of N-HCNF-2-1000. Methanol tolerance was another important parameter for ORR catalysts. To examine the methanol crossover effects, 1 M methanol was injected into the electrolyte during the potential static test. As shown in Fig. S7f,† no obvious change of the current density of N-HCNF-2-1000 was observed, indicating that N-HCNF-2-1000 showed excellent methanol tolerance. Furthermore, after more than 50 000 seconds of current–time chronoamperometry test, N-HCNF-2-1000 showed only a 4% current decrease while 17% current loss was observed for Pt/C, indicating superior durability of the as-obtained N-HCNF-2-1000 (Fig. 3c). It was further verified by its very small negative shift of half-potential (23 mV) after 10 000 CV cycles (Fig. S9†).

To demonstrate the dual-function of N-CHNFs, we observed high HER activities in N_2-saturated 0.5 M H_2SO_4 electrolyte solution. The corresponding results are depicted in Fig. 3d–f and Fig. S10 and 11,† and the corresponding samples exhibit greatly high HER activity. To be specific, the over-potentials to achieve a current density of 10 mA cm^{-2} for the N-HCNF-1-1000, N-HCNF-2-1000, and N-HCNF-3-1000 were −356 mV, −243 mV, and −294 mV *vs.* RHE, indicating that the contents of CTF-PP greatly influence the HER performance (Fig. 3d). An excellent performance might stem from a suitable CTF-PP introduction, which could also tailor the N-active sites of the resultant carbon-based materials. However, excessive CTF-PP accumulation would decrease the pore volume, which would cause the decline of electrocatalytic activity. Remarkably, N-HCNF-2-1000 shows superior HER performance with almost the same positive E_{onset} as Pt/C (−0.03 V), which is much more positive than that of the other as-prepared samples in this work. The excellent kinetic property of N-HCNF-2-1000 is confirmed by its small Tafel slope of 111 mV dec^{-1} (Fig. 3e). The excellent stability of N-HCNF-2-1000 was further verified by its small increase of over-potential after 5000 CV cycles (Fig. 3f) and a consistent HER current after 16 h of continuous operation at −0.25 V (Fig. S10a†). Therefore, the N-HCNF-2-1000 with a low onset potential, small Tafel slope, and long-term stability is a very promising catalyst for the HER. The electrochemical surface areas (ESAs) were determined by the double-layer capacitance that can be measured by CVs, reflecting the exposed active sites. Fig. S10b† illustrates the CVs of N-HCNF-2-1000 at different scan rates in 0.5 M H_2SO_4 media which were determined by the non-faradaic capacitive current. The corresponding linear plot for determining the C_{DL} of N-HCNF-2-1000 and the linear slope (C_{DL}) of N-HCNF-2-1000 showed 11.22 mF cm^{-2} and −10.97 mF cm^{-2} (Fig. S10c†), higher than those of N-HCNF-2-1100 (6.66 mF cm^{-2} and −6.89 mF cm^{-2}) and N-HCNF-2-900 (5.09 mF cm^{-2} and −4.76 mF cm^{-2}) (Fig. S11†). These results further indicated that N-HCNF-2-1000 shows an outstanding performance for hydrogen evolution. In addition, to further inspect the surface-evolution process of the N-HCNF-2-1000 catalyst, we characterized the composition and morphology of the as-obtained catalyst after the stability test. SEM and TEM observation revealed that the microstructure is basically unchanged after the stability test (as shown in Fig. S12a–c†). Elemental mapping images

(Fig. S12d†) reveal that a tremendous amount of nitrogen still exists and homogeneously distributes in the carbon matrix, demonstrating that the as-prepared material has good structural stability. Fig. S13a† shows the XRD pattern of the N-HCNF-2-1000 after the stability test, which still corresponds to the (002) peak and (010) peak, indicating that the hollow carbon structures have good chemical stability. According to the Raman spectra (Fig. S13b†), after the stability test, the ratio of the relative intensity between the D band and G band slightly increased to 0.96, which is mainly attributed to the slight corrosion of carbon during the testing process.

A primary Zn–air battery was constructed to evaluate the performance of N-HCNF-2-1000 when used as a catalyst in actual battery operation (Fig. 4a). The assembled Zn–air battery has a high open-circle voltage of 1.45 V, which approaches the 1.50 V of the commercial Pt/C(Fig. S14a†). The polarization and power density curves of the N-HCNF-2-1000 based Zn–air battery (Fig. 4b) deliver a current density of 212 mA cm^{-2} at a peak power density of 136 mW cm^{-2}, superior to the Pt/C catalyst with a current density of 193 mA cm^{-2} at a peak power density of 115 mW cm^{-2}.[47] The N-HCNF-2-1000 catalyst provides an excellent max-power density compared to most of the nonprecious metal catalysts in the literature (summarized in Fig. S14b†), suggesting its great potential for application in energy conversion. Notably, the galvanostatic discharge voltage curves of the N-HCNF-2-1000 and Pt/C catalyst air electrode at a discharge current density of 20 mA cm^{-2} are shown in Fig. 4c; the voltage of the Zn–air battery employing the N-HCNF-2-1000 air cathode is parallel to that of the commercial Pt/C air cathode with no obvious voltage drop. The specific capacity of the as-made Zn–air battery employing the N-HCNF-2-1000 air cathode is more than 780 mA h g^{-1} at a discharge current density of 20 mA cm^{-2}, normalized to the consumed Zn plate, which is significantly higher than the 718 mA h g^{-1} of the Pt/C electrode with the same discharge current density. Fig. 4d depicts the rate capability performance of the Zn–air batteries with the N-HCNF-2-1000 and Pt/C air cathodes with the increase of discharge current densities from 0 to 50 and then returning to the original current density of 0 mA cm^{-2}. The self-made primary Zn–air battery with the N-HCNF-2-1000 air electrode possessed an outstanding rate behavior than the commercial Pt/C-based air electrode. As shown in Fig. S14a,† when two Zn–air batteries are connected in series, the motor can be driven to rotate rapidly for a long time. Furthermore, the max-power density of the N-HCNF-2-1000 is higher than that of the most reported catalysts. All these above results verify the excellent catalytic performance of N-HCNF-2-1000 which can meet the needs of practical applications.

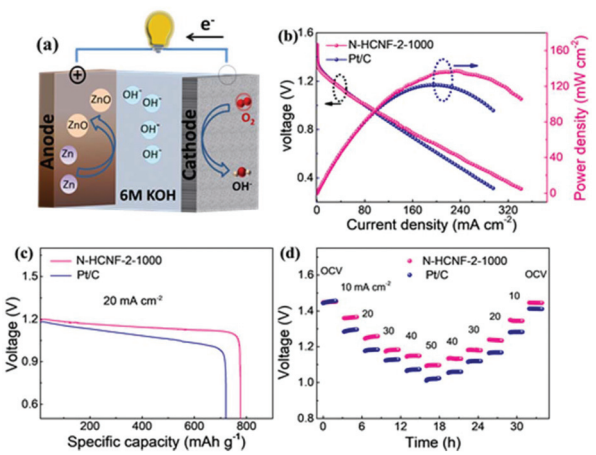

Fig. 4 (a) Schematic for the fabrication of the zinc–air battery, (b) polarization curves and power densities of N-HCNF-2-1000 and Pt/C cathodes, respectively, (c) galvanostatic discharge curves of N-HCNF-2-1000 and Pt/C cathodes at a discharge current density of 20 mA cm^{-2}, respectively, and (d) rate capability of N-HCNF-2-1000 and Pt/C cathodes at different current densities.

Conclusions

In summary, we have developed a simple route to fabricate N-doped hollow carbon materials by a step-wise polymerization and subsequent pyrolysis procedure. A preformed covalent triazine framework as a precursor was controllably grown on the surface of the MCA crystal by pre-covalent linking. The ideal hollow structure, sufficient N-doped active sites and high SSA led to efficient and durable bifunctional electrocatalytic activity for the ORR and HER. This strategy provides a promising method for designing multifunctional materials for energy conversion and storage.

Conflicts of interest

There are no conflicts to declare.

Acknowledgements

We are grateful for the financial support from the National Natural Science Foundation of China (51773035), the Natural Science Foundation of Shanghai (17ZR1439900), the Program of Shanghai Subject Chief Scientist (17XD1400100), and the Shanghai Scientific and Technological Innovation Project (18JC1410600).

Notes and references

1 Y. Li and H. Dai, *Chem. Soc. Rev.*, 2014, **43**, 5257–5275.
2 K. Gong, F. Du, Z. Xia, M. Durstock and L. Dai, *Science*, 2009, **323**, 760–764.
3 J. Shui, M. Wang, F. Du and L. Dai, *Sci. Adv.*, 2015, **1**, 1400129.
4 Y. Zheng, Y. Jiao, L. H. Li, T. Xing, Y. Chen, M. Jaroniec and S. Z. Qiao, *ACS Nano*, 2014, **8**, 5290–5296.
5 S. Li, Z. Cui, D. Li, G. Yue, J. Liu, H. Ding, S. Gao, Y. Zhao, N. Wang and Y. Zhao, *Compos. Commun.*, 2019, **13**, 1–11.

6 X. Tian, X. Zhao, Y.-Q. Su, L. Wang, H. Wang, D. Dang, B. Chi, H. Liu, E. J. M. Hensen, X. W. Lou and B. Y. Xia, *Science*, 2019, **366**, 850.
7 Z.-L. Wang, D. Xu, J.-J. Xu and X.-B. Zhang, *Chem. Soc. Rev.*, 2014, **43**, 7746–7786.
8 J. Yi, P. Liang, X. Liu, K. Wu, Y. Liu, Y. Wang, Y. Xia and J. Zhang, *Energy Environ. Sci.*, 2018, **11**, 3075–3095.
9 H. Guo, J. Zhou, Q. Li, Y. Li, W. Zong, J. Zhu, J. Xu, C. Zhang and T. Liu, *Adv. Funct. Mater.*, 2020, **30**, 2000024.
10 M. Shao, Q. Chang, J.-P. Dodelet and R. Chenitz, *Chem. Rev.*, 2016, **116**, 3594–3657.
11 H. Guo, Q. Feng, K. Xu, J. Xu, J. Zhu, C. Zhang and T. Liu, *Adv. Funct. Mater.*, 2019, **29**, 1903660.
12 Y. Chen, Y. Li, F. Yao, C. Peng, C. Cao, Y. Feng and W. Feng, *Sustainable Energy Fuels*, 2019, **3**, 2237–2245.
13 S. Huang, Y. Li, Y. Feng, H. An, P. Long, C. Qin and W. Feng, *J. Mater. Chem. A*, 2015, **3**, 23095–23105.
14 Q. Liu, J. Shen, X. Yu, X. Yang, W. Liu, J. Yang, H. Tang, H. Xu, H. Li, Y. Li and J. Xu, *Appl. Catal., B*, 2019, **248**, 84–94.
15 S. G. Peera, A. K. Sahu, A. Arunchander, S. D. Bhat, J. Karthikeyan and P. Murugan, *Carbon*, 2015, **93**, 130–142.
16 S. Jiang, Y. Sun, H. Dai, J. Hu, P. Ni, Y. Wang, Z. Li and Z. Li, *Nanoscale*, 2015, **7**, 10584–10589.
17 S. Chen, J. Bi, Y. Zhao, L. Yang, C. Zhang, Y. Ma, Q. Wu, X. Wang and Z. Hu, *Adv. Mater.*, 2012, **24**, 5593–5597.
18 W. A. Saidi, *J. Phys. Chem. Lett.*, 2013, **4**, 4160–4165.
19 H. An, Y. Li, Y. Gao, C. Cao, J. Han, Y. Feng and W. Feng, *Carbon*, 2017, **116**, 338–346.
20 H. Tan, J. Tang, J. Henzie, Y. Li, X. Xu, T. Chen, Z. Wang, J. Wang, Y. Ide, Y. Bando and Y. Yamauchi, *ACS Nano*, 2018, **12**, 5674–5683.
21 F. Liu, X. Cheng, R. Xu, Y. Wu, Y. Jiang and Y. Yu, *Adv. Funct. Mater.*, 2018, **28**, 1800394.
22 Y. Han, Y.-G. Wang, W. Chen, R. Xu, L. Zheng, J. Zhang, J. Luo, R.-A. Shen, Y. Zhu, W.-C. Cheong, C. Chen, Q. Peng, D. Wang and Y. Li, *J. Am. Chem. Soc.*, 2017, **139**, 17269–17272.
23 S. Pedireddy, H. K. Lee, W. W. Tjiu, I. Y. Phang, H. R. Tan, S. Q. Chua, C. Troadec and X. Y. Ling, *Nat. Commun.*, 2014, **5**, 4947.
24 M. Jafarzadeh, C. S. Sipaut, J. Dayou and R. F. Mansa, *Renewable Sustainable Energy Rev.*, 2016, **64**, 543–568.
25 S. Li, C. Cheng, X. Zhao, J. Schmidt and A. Thomas, *Angew. Chem.*, 2018, **130**, 1874–1880.
26 H.-J. Kang, Y. S. Huh, W. B. Im and Y.-S. Jun, *ACS Nano*, 2019, **13**, 11935–11946.
27 J. H. Kim, M. Byeon, Y. C. Jeong, J. Y. Oh, Y. Jung, N. Fechler, S. J. Yang and C. R. Park, *J. Mater. Chem. A*, 2017, **5**, 20635–20642.
28 B. Zhou, L. Liu, P. Cai, G. Zeng, X. Li, Z. Wen and L. Chen, *J. Mater. Chem. A*, 2017, **5**, 22163–22169.
29 B. C. Patra, S. Khilari, R. N. Manna, S. Mondal, D. Pradhan, A. Pradhan and A. Bhaumik, *ACS Catal.*, 2017, **7**, 6120–6127.
30 W. Ding, L. Li, K. Xiong, Y. Wang, W. Li, Y. Nie, S. Chen, X. Qi and Z. Wei, *J. Am. Chem. Soc.*, 2015, **137**, 5414–5420.
31 M. Wu, Y. Zhao, B. Sun, Z. Sun, C. Li, Y. Han, L. Xu, Z. Ge, Y. Ren, M. Zhang, Q. Zhang, Y. Lu, W. Wang, Y. Ma and Y. Chen, *Nano Energy*, 2020, **70**, 104498.
32 X. Cui, S. Lei, A. C. Wang, L. Gao, Q. Zhang, Y. Yang and Z. Lin, *Nano Energy*, 2020, 104525.
33 G. Lu, Y. Zhu, K. Xu, Y. Jin, Z. J. Ren, Z. Liu and W. Zhang, *Nanoscale*, 2015, **7**, 18271–18277.
34 H. Zhao, G. Yu, M. Yuan, J. Yang, D. Xu and Z. Dong, *Nanoscale*, 2018, **10**, 21466–21474.
35 D. Meng, J. Fan, J. Ma, S.-W. Du and J. Geng, *Compos. Commun.*, 2019, **12**, 64–73.
36 J. Liu, Y. Hu and J. Cao, *Catal. Commun.*, 2015, **66**, 91–94.
37 L. Hao, S. Zhang, R. Liu, J. Ning, G. Zhang and L. Zhi, *Adv. Mater.*, 2015, **27**, 3189–3189.
38 L. Jiao, Y. Hu, H. Ju, C. Wang, M.-R. Gao, Q. Yang, J. Zhu, S.-H. Yu and H.-L. Jiang, *J. Mater. Chem. A*, 2017, **5**, 23170–23178.
39 P. Puthiaraj, Y.-R. Lee, S. Zhang and W.-S. Ahn, *J. Mater. Chem. A*, 2016, **4**, 16288–16311.
40 S. Chen, Y. Zheng, B. Zhang, Y. Feng, J. Zhu, J. Xu, C. Zhang, W. Feng and T. Liu, *ACS Appl. Mater. Interfaces*, 2019, **11**, 1384–1393.
41 S. N. Talapaneni, T. H. Hwang, S. H. Je, O. Buyukcakir, J. W. Choi and A. Coskun, *Angew. Chem., Int. Ed.*, 2016, **55**, 3106–3111.
42 S. Chen, J. Cheng, L. Ma, S. Zhou, X. Xu, C. Zhi, W. Zhang, L. Zhi and J. A. Zapien, *Nanoscale*, 2018, **10**, 10412–10419.
43 Y. Lv, L. Yang and D. Cao, *ACS Appl. Mater. Interfaces*, 2017, **9**, 32859–32867.
44 X. Zhu, L. Mo, Y. Wu, F. Lai, X. Han, X. Y. Ling, T. Liu and Y.-E. Miao, *Compos. Commun.*, 2018, **9**, 86–91.
45 S. Huang, Y. Meng, Y. Cao, S. He, X. Li, S. Tong and M. Wu, *Appl. Catal., B*, 2019, **248**, 239–248.
46 X. Guo, P. Liu, J. Han, Y. Ito, A. Hirata, T. Fujita and M. Chen, *Adv. Mater.*, 2015, **27**, 6137–6143.
47 S. Chen, S. Chen, B. Zhang and J. Zhang, *ACS Appl. Mater. Interfaces*, 2019, **11**, 16720–16728.
48 J. Gao, Y. Wang, H. Wu, X. Liu, L. Wang, Q. Yu, A. Li, H. Wang, C. Song, Z. Gao, M. Peng, M. Zhang, N. Ma, J. Wang, W. Zhou, G. Wang, Z. Yin and D. Ma, *Angew. Chem., Int. Ed.*, 2019, **58**, 2–11.
49 J. Guo, T. Li, Q. Wang, N. Zhang, Y. Cheng and Z. Xiang, *Nanoscale*, 2019, **11**, 211–218.